RESEARCH ARTICLE | SEPTEMBER 10 2024

Dynamics of an acoustically levitated fluid droplet captured by a low-order immersed boundary method

Jacqueline B. Sustiel ; David G. Grier

Physics of Fluids 36, 092108 (2024)
https://doi.org/10.1063/5.0223790
CHORUS

Physics of Fluids ARTICLE pubs.aip.org/aip/pof

Dynamics of an acoustically levitated fluid droplet captured by a low-order immersed boundary method

Cite as: Phys. Fluids **36**, 092108 (2024); doi: 10.1063/5.0223790
Submitted: 17 June 2024 · Accepted: 18 August 2024 ·
Published Online: 10 September 2024

View Online Export Citation CrossMark

Jacqueline B. Sustiel and David G. Grier[a)]

AFFILIATIONS

Department of Physics and Center for Soft Matter Research, New York University, New York, New York 10003, USA

[a)]Author to whom correspondence should be addressed: david.grier@nyu.edu

ABSTRACT

We present a variant of the immersed boundary (IB) method that implements acoustic perturbation theory to model acoustically levitated fluid droplets. Instead of resolving sound waves numerically, our hybrid method solves acoustic scattering semi-analytically to obtain the corresponding time-averaged acoustic forces on the droplet. This framework allows the droplet to be simulated on inertial timescales of interest, and therefore works with much larger time steps than traditional compressible flow solvers. To benchmark this technique and demonstrate its utility, we implement the hybrid IB method for a single droplet in a standing wave. Simulated droplet shape deformations and streaming profiles agree with available theoretical predictions. Our simulations also yield insights into the streaming profiles for elliptical droplets, for which a comprehensive analytic solution does not yet exist.

NOMENCLATURE

Droplet properties

$\mathbf{F}_i$	Force on boundary marker
K_P	Spring constant between mass marker and tracer
ℓ_i	Separation between markers i and $i+1$
M	Mass of mass marker
R	Undeformed droplet radius
$r(\theta)$	Deformed droplet radius, Eq. (32)
$\mathbf{U}_i$	Velocity of boundary marker
$\mathbf{X}_i$	Position of boundary marker
$\mathbf{X}_i^m$	Position of massless (fluid) tracer marker
$x_{\ell m}$	Deformation coefficients, Eq. (33)
$\mathbf{Y}_i^m$	Position of mass marker
ρ_p	Droplet's density
σ	Interfacial tension

Medium properties

c	Speed of sound
$\mathbf{f}(\mathbf{x}_j)$	Force on fluid, Eq. (1)
h	Grid spacing
$p(\mathbf{x}_j)$	Fluid pressure, Eq. (1)
$\mathbf{u}(\mathbf{x}_j)$	Fluid velocity, Eq. (1)
$\mathbf{x}_j$	Location on computational grid
$\delta_h(\mathbf{x}_j - \mathbf{X}_i)$	Interpolation kernel between grid and markers, Eq. (A5)
η	Fluid's dynamic viscosity
ξ	Fluid's volume viscosity
$\rho(\mathbf{x}_j)$	Fluid density, Eq. (1)
ρ_0	Fluid's equilibrium density

Acoustic wave properties

a_ℓ^m	Scattered beam shape coefficients, Eq. (18)
b_ℓ^m	Interior beam shape coefficients, Eq. (18)
k	Wavenumber
k_ν	Viscous wavenumber, Eq. (16)
s_ℓ^m	Scattered beam shape coefficients, Eq. (18)
γ	Acoustic damping coefficient, Eq. (15)
$\delta(\omega)$	Viscous boundary layer thickness, Eq. (17)
$\phi(\mathbf{x}_j)$	Flow field scalar potential, Eq. (13)
$\boldsymbol{\psi}(\mathbf{x}_j)$	Flow field vector potential, Eq. (13)
ω	Frequency

I. INTRODUCTION

Acoustic manipulation uses the forces exerted by sound waves to lift objects against gravity and to move them along planned trajectories in three dimensions.[1–5] The theory of acoustic manipulation is

well-developed for solid objects in inviscid fluids.[6] The behavior of deformable objects, however, poses more of a challenge. Acoustic scattering and sound-mediated shape changes occur on dramatically different time scales, making their interplay difficult to model self-consistently.[7,8] The standard formulation of sound-mediated forces and flows is based on second-order perturbation theory. The first-order pressure and velocity fields, $p_1(\mathbf{r},t)$ and $\mathbf{u}_1(\mathbf{r},t)$, respectively, describe incident sound waves together with waves scattered by particles. These first-order fields oscillate harmonically at the acoustic frequency, ω, and vanish on average. Their interference, however, gives rise to steady acoustic radiation forces (ARF)[9] and streaming flows[10–14] at second order in the amplitude of the sound wave. This wave-matter interaction has been formulated analytically for highly symmetric scatterers[6,14–17] and semi-analytically for scatterers of fixed arbitrary shape.[18] Even numerical solutions are challenging, however, for scatterers whose shape can change.

Here, we introduce an efficient computational framework based on the immersed boundary (IB) method[19,20] that accurately predicts the dynamics and shape evolution of fluid droplets in acoustic force landscapes, as well as the streaming flows around them. The IB method naturally accommodates the moving boundary of a deformable droplet and couples it to flows in the fluid medium. We then couple this dynamical system semi-analytically to an acoustic pressure wave by projecting the time-averaged acoustic force at the deformed droplet's surface onto the incompressible flow around an equivalent sphere. This framework models acoustic levitation substantially more efficiently than existing compressible-flow solvers by inherently accommodating both fast and slow processes. We validate this hybrid numerical framework by studying shape deformations and flow fields around fluid droplets in an acoustic levitator. This study identifies a dynamical transition between dipolar and quadrupolar streaming flows that may explain anomalous collective phenomena in experimental studies of acoustically levitated droplets[5] and can be useful for designing microfluidic devices.[21]

Section II reviews the standard IB method[20] along with extensions that incorporate the mass and surface tension of a fluid droplet. Acoustic forces and streaming flows are derived in Sec. III from acoustic perturbation theory. Section IV presents a hybrid IB method that models the acoustic forces on a droplet in a standing sound wave. The results compare well with the best available multiscale computational studies and are obtained at a fraction of the computational cost.

II. IMMERSED BOUNDARY METHOD

The immersed boundary method was first introduced in 1972 to study blood flow in the heart,[19] and has since evolved into a general method for solving fluid–structure interaction problems.[20] Modeling fluid droplets involves a variant of this technique called the penalty immersed boundary method that incorporates the droplets' mass and surface tension.[22,23] The present work further extends the penalty IB method by incorporating the forces exerted by an acoustic wave propagating through the fluid medium.

A. The standard IB method

The standard formulation of the IB method[20] applies to a droplet embedded in a homogeneous incompressible fluid of density ρ and dynamic viscosity η. The droplet's surface, $\mathbf{X}(\mathbf{q})$, is parameterized by curvilinear coordinates, $\mathbf{q}$, and is discretized into a set of markers, $\{\mathbf{X}_i\}$, at fixed material points along the boundary, as shown schematically in Fig. 1.

The fluid flow, $\mathbf{u}(\mathbf{x}_j)$, and pressure, $p(\mathbf{x}_j)$, are defined on a Cartesian grid, $\mathbf{x}_j$, with uniform spacing h, and are governed by the viscous, incompressible Navier–Stokes equations,

$$\rho\left(\partial_t + \mathbf{u}\cdot\nabla\right)\mathbf{u} = -\nabla p + \eta\nabla^2\mathbf{u} + \mathbf{f}, \tag{1a}$$

$$\nabla\cdot\mathbf{u} = 0. \tag{1b}$$

By Newton's third law, the force on the fluid element at $\mathbf{x}_j$,

$$\mathbf{f}(\mathbf{x}_j,t) = -\int \mathbf{F}(\mathbf{q},t)\,\delta_h(\mathbf{x}_j - \mathbf{X}(\mathbf{q},t))\,d\mathbf{q}, \tag{2}$$

is equal and opposite to the local force on the boundary, $\mathbf{F}(\mathbf{q},t)$, due to surface tension and the influence of external fields. The kernel, $\delta_h(\mathbf{x}_j - \mathbf{X}_i)$, interpolates over the markers, $\mathbf{X}_i$, in the neighborhood of a discrete gridpoint, $\mathbf{x}_j$. A suitable interpolation kernel is presented in Appendix A. Likewise, each massless boundary marker is advected by the fluid at a velocity,

$$\mathbf{U}_i = \int \mathbf{u}(\mathbf{x}_j,t)\,\delta_h(\mathbf{x}_j - \mathbf{X}_i)\,d\mathbf{x}_j, \tag{3}$$

that is interpolated from the computational grid.

The IB method defined by Eqs. (1)–(3) generally proceeds in a cycle, as depicted in Fig. 2. Given an initial droplet shape, $\{\mathbf{X}_i\}$, the forces, $\{\mathbf{F}_i\}$, on the boundary markers are calculated from the combined influences of surface tension and external forces. The complementary force field acting on the fluid, $\mathbf{f}(\mathbf{x}_j,t)$, is then computed with Eq. (2). The Navier–Stokes equations, Eq. (1), then are solved numerically[19,20] to obtain the updated fluid velocity, $\mathbf{u}(\mathbf{x}_j,t)$. Finally, Eq. (3) is used to determine the no-slip motion of the boundary, $\partial_t\mathbf{X} = \mathbf{U}$, and the procedure is repeated for the updated boundary configuration, $\{\mathbf{X}_j\}$.

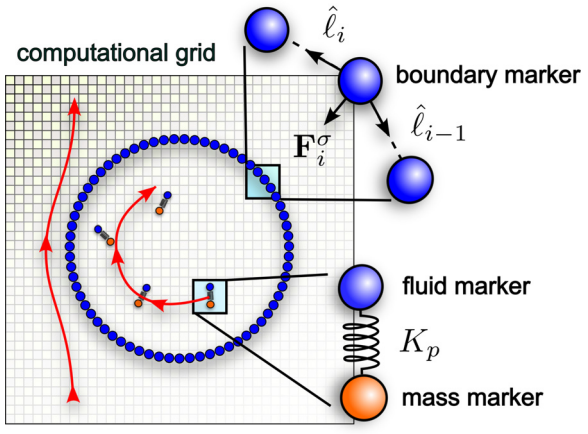

FIG. 1. Schematic overview of the immersed boundary method applied to a fluid droplet driven by an acoustic pressure field. Boundary markers are located at positions, $\mathbf{X}_i(\mathbf{q})$, around the droplet's interface. Each marker interacts with its neighbors to model the interfacial restoring force, $\mathbf{F}_i^\sigma$. Each marker also interacts with flows in the fluid medium that are calculated on the computational grid. The droplet's density is modified through the addition of mass markers that are coupled to the flow field by fluid markers.

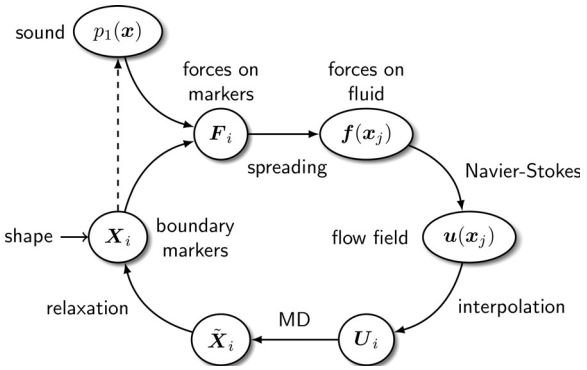

FIG. 2. Immersed Boundary method for acoustic manipulation of deformable objects. The computational cycle begins by specifying an initial shape for the droplet and the incident sound field.

In this work, we implement the same numerical scheme first introduced by Peskin,[19] using the spatial and temporal discretizations and four-point discrete delta function described in Secs. 4–7 of Ref. 20. To improve volume conservation, we calculate the fluid fields on a staggered, marker-and-cell grid.[24] The expressions used for spatiotemporal discretization are reproduced in Appendix A.

B. Penalty IB method for massive droplets

The standard IB method cannot account for multiphase flows where properties of the droplet, such as density and viscoelasticity, differ from those of the surrounding medium.[24] For simplicity, we focus on the droplet's density contrast relative to the medium. To incorporate the droplet's excess mass, we implement an extension of the IB method based on the penalty immersed boundary method.[22,25]

The penalty IB method models the density of the droplet interior by introducing a set of massless tracer particles at locations $\{\mathbf{X}_i^m\}$ whose trajectories trivially satisfy Eqs. (1)–(3). As shown in Fig. 1, each of these fluid markers is coupled to a corresponding *mass marker* at position $\mathbf{Y}_i^m$ by a spring of stiffness K_P. The ith fluid marker experiences a force,

$$\mathbf{F}_i^m = K_P\left(\mathbf{Y}_i^m - \mathbf{X}_i^m\right), \tag{4}$$

that accelerates it according to Newton's second law,

$$M\,\partial_t^2\mathbf{Y}_i^m = -\mathbf{F}_i^m - Mg\hat{z}, \tag{5}$$

where M is the marker's mass and g is the acceleration due to gravity.

In isolation, the mass markers obeys rigid body dynamics, and the IB markers constitutes tracer particles in the fluid. The trajectory of each mass marker is related to its respective IB marker only through the penalty force between them. The spring force in Eq. (5) introduces inertial fluid forces into the mass markers' rigid body dynamics. Likewise, the same spring force on the IB markers from Eq. (4) is spread to the fluid via Eq. (2), thereby ensuring body forces on the mass markers are translated to the fluid.

In theory, the fluid markers and mass markers ought to coincide in the limit of large K_P. In practice, however, numerical instability arises when K_P is too large. Consequently, K_P is chosen phenomenologically to maintain pair separations smaller than the computational grid size, typically at $h/10$.

C. Surface tension

The internal boundary stress on a marker at $\mathbf{X}_i$ is often formulated as a restoring force, $\mathbf{F}_i = -\nabla_{\mathbf{X}_j}E$, that minimizes the interfacial energy, $E[\{\mathbf{X}_j\}]$. When this approach is used to model surface tension, the interfacial energy is proportional to the droplet's total surface area. In two dimensions, it is proportional to the length of the interface,

$$E\left[\{\mathbf{X}_j\}\right] = \sigma A = \sigma\sum_{j=1}^{N_{ib}-1}||\ell_j||, \tag{6}$$

where $\ell_j \equiv \mathbf{X}_{j+1} - \mathbf{X}_j$, and σ is the interfacial tension. The force of surface tension acting on the marker is then

$$\mathbf{F}_i^\sigma = -\sigma(\hat{\ell}_i - \hat{\ell}_{i-1}). \tag{7}$$

Equation (7) correctly models surface tension if the boundary markers are uniformly distributed around the droplet's boundary. To this end, the markers are redistributed tangentially along the boundary at each time step.

Surface tension exerts a normal force on the droplet surface to minimize local curvature. Consequently, Eq. (7) also defines the surface normal, $\hat{\mathbf{n}}_i = \mathbf{F}_i^\sigma/||\mathbf{F}_i^\sigma||$.

D. Benchmark: Sedimenting droplet

To demonstrate and benchmark our implementation of the IB method, we model the sedimentation of a droplet in an unbounded fluid.[23] Figure 3 presents a cross-section of the flow around and within a droplet of radius $R = 4\,\mu$m and buoyant density

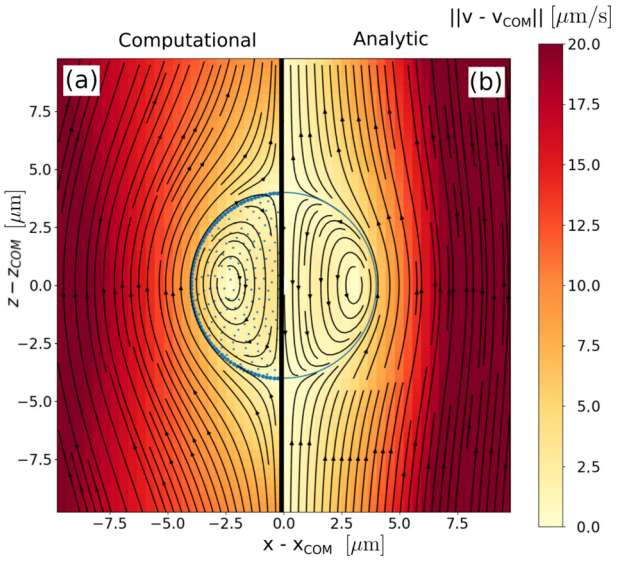

FIG. 3. Streamlines within and around an 8 μm-diameter droplet falling through an unbounded fluid at its terminal velocity, $\approx 20\,\mu$m s^{-1}. We compare (a) simulations using a penalty Immersed Boundary method for the droplet's excess mass to (b) the analytic stream function from Happel and Brenner.[26]

$\rho_p - \rho_0 = 0.18\,\mathrm{g\,cm^{-3}}$, which corresponds to silicone oil sedimenting in water.[5] For simplicity, we assume the fluid droplet has the same viscosity as the surrounding medium. The plot shows streamlines of the flow in the co-moving frame and is colored by the local flow speed. The data in Fig. 3(a) are computed with the IB method in a $20 \times 20\,\mu\mathrm{m}^2$ periodic domain. They are compared side-by-side with the analytic result for a spherical droplet[26] in Fig. 3(b). This solution for the two-phase flow is reproduced in Appendix B. Slight differences between the two flow fields can be attributed to the influence of periodic boundary conditions on the simulations and to the implicit assumption of infinite surface tension in the analytic model.

III. ACOUSTICS

The standard IB method relies on the incompressible Navier–Stokes equations, Eq. (1), and therefore does not accommodate sound waves. Describing the fields within an acoustic levitator requires the compressible Navier–Stokes equations,

$$\partial_t \rho = -\nabla \cdot (\rho \mathbf{u}), \tag{8a}$$

$$\rho\,(\partial_t + \mathbf{u}\cdot\nabla)\,\mathbf{u} = -\nabla p + \eta\,\nabla^2\mathbf{u} + \beta\eta\,\nabla(\nabla\cdot\mathbf{u}), \tag{8b}$$

where $\beta = \xi/\eta + 1/3$ incorporates the fluid's volume viscosity, ξ.[14,27]

In the absence of sound waves, the fluid medium is quiescent, $\mathbf{u} = 0$, and has uniform pressure p_0, and uniform density, ρ_0. An acoustic levitator projects a time-harmonic pressure wave, $p_{\mathrm{inc}}(\mathbf{x}, t) = p_{\mathrm{inc}}(\mathbf{x})\exp(-i\omega t)$, into the fluid. The droplet scatters a portion of p_{inc} to create a scattered wave, $p_{\mathrm{scat}}(\mathbf{x}, t) = p_{\mathrm{scat}}(\mathbf{x}, \{\mathbf{X}_j\})\exp(-i\omega t)$, that depends on the position and shape of the droplet. The incident and scattered waves together cause small pressure fluctuations, $p_1(\mathbf{x}) = p_{\mathrm{inc}}(\mathbf{x}) + p_{\mathrm{scat}}(\mathbf{x})$, about p_0. This first-order pressure wave is associated with a first-order density wave, $\rho_1(\mathbf{x})$, and a first-order velocity field, $\mathbf{u}_1(\mathbf{x})$, that are obtained by expanding Eq. (8) to first order in the fields.

Acoustic levitators typically operate at such high frequencies that the period of $p_1(\mathbf{x}, t)$ is much shorter than the viscous and inertial time scales that govern droplet dynamics and streaming flows. Those comparatively slow processes emerge as averages over multiple acoustic cycles. Because the first-order fields are harmonic and therefore vanish on average, standard acoustic perturbation theory[9] expands the density, pressure, and velocity fields to second order,

$$\rho = \rho_0 + \rho_1 + \rho_2, \tag{9a}$$

$$p = p_0 + p_1 + p_2, \tag{9b}$$

$$\mathbf{u} = \mathbf{u}_1 + \mathbf{u}_2. \tag{9c}$$

The second-order fields, ρ_2, p_2, and $\mathbf{u}_2$, do not vanish on average and therefore describe steady dynamics that persist on hydrodynamic timescales and therefore account for the droplet's macroscopic behavior.

We extend the IB method to incorporate sound waves by identifying the time-averaged acoustic radiation force (ARF) on each element of the droplet surface,[6,7,9,28,29]

$$\mathbf{F}_i^{ARF}(t) = -\langle p_2\rangle\hat{\mathbf{n}} - \rho_0\langle(\mathbf{u}_1\cdot\hat{\mathbf{n}})\,\mathbf{u}_1\rangle, \tag{10}$$

where the continuous fields are evaluated at $\mathbf{x} = \mathbf{X}_i$ and angle brackets represent an average over one acoustic cycle. The first term on the right-hand side of Eq. (10) describes the acoustic radiation pressure, and the second term arises from advection of the fluid by the droplet's oscillating boundary.[7,28]

The net force on the boundary marker at $\mathbf{X}_i$,

$$\mathbf{F}_i(t) = \mathbf{F}_i^{ST}(t) + \mathbf{F}_i^{ARF}(t), \tag{11}$$

is the sum of the surface tension from Eq. (7) and the time-averaged acoustic radiation force from Eq. (10). The interfacial force drives streaming flows, $\langle\mathbf{u}(\mathbf{x}_j, t)\rangle = \mathbf{u}_2(\mathbf{x}, t)$, and shape deformations, $\partial_t\mathbf{X}_i = \mathbf{U}_i$, through the cycle depicted in Fig. 2. This extension to the incompressible IB method is one of the principal contributions of the present work. Its implementation requires expressions for the first- and second-order fields.

A. First-order equations for the acoustic wave

The first-order Navier–Stokes equations,

$$\partial_t\rho_1 = -\rho_0\,\nabla\cdot\mathbf{u}_1, \tag{12a}$$

$$\rho_0\,\partial_t\mathbf{u}_1 = -\nabla p_1 + \eta\,(\beta+1)\nabla(\nabla\cdot\mathbf{u}_1) - \eta\,\nabla\times\nabla\times\mathbf{u}_1, \tag{12b}$$

can be simplified to a pair of wave equations,

$$\nabla^2\phi = -\frac{k^2}{\gamma}\,\phi, \tag{13a}$$

$$\nabla\times\nabla\times\boldsymbol{\psi} = k_\nu^2\boldsymbol{\psi}, \tag{13b}$$

by introducing the Helmholtz decomposition,

$$\mathbf{u}_1(\mathbf{r}) = \nabla\phi + \nabla\times\boldsymbol{\psi}, \tag{14a}$$

$$p_1(\mathbf{r}) = i\frac{\omega\rho_0}{\gamma}\,\phi(\mathbf{r}), \tag{14b}$$

and noting that $p_1(\mathbf{r}) = c_0^2\,\rho_1(\mathbf{r})$ in an isentropic fluid with speed of sound c_0. Equation (13a) describes a scalar pressure wave that propagates with the acoustic wavenumber, $k = \omega/c_0$. Likewise, Eq. (13b) describes vortical waves that carry away the acoustic energy lost to viscous damping. The acoustic damping coefficient,

$$\gamma = 1 + (\beta+1)\left(\frac{k}{k_\nu}\right)^2, \tag{15}$$

and the viscous wave number,

$$k_\nu = \frac{1+i}{\delta}, \tag{16}$$

are both characterized by the thickness of the viscous boundary layer,[27]

$$\delta(\omega) = \sqrt{\frac{2\eta}{\rho_0}\frac{1}{\omega}}. \tag{17}$$

Following conventional acoustic radiation theory,[5,27] we neglect viscosity in the first-order fields, so that $\gamma \approx 1$ and $\boldsymbol{\psi} \approx \mathbf{0}$. The solution to Eq. (13) can then be found by a multipole expansion of $\phi(\mathbf{r})$ both inside and outside the droplet,[30]

$$\phi_{\mathrm{I}}(\mathbf{r}) = \phi_0\sum_{\ell=0}^{\infty}\sum_{m=-\ell}^{\ell} b_\ell^m\,j_\ell(k_{\mathrm{I}}r)\,P_\ell^m(\cos\theta) \tag{18a}$$

and

$$\phi_{\mathrm{O}}(\mathbf{r}) = \phi_0\sum_{\ell=0}^{\infty}\sum_{m=-\ell}^{\ell} a_\ell^m\left[j_\ell(kr) + s_\ell^m h_\ell(kr)\right]P_\ell^m(\cos\theta), \tag{18b}$$

respectively, where j_ℓ and h_ℓ are the spherical Bessel and Hankel functions, respectively, and P_ℓ^m is the associated Legendre polynomial. Distances in Eq. (18a) are scaled by the wavenumber inside the droplet, $k_\mathrm{I} = \omega/c_\mathrm{I}$.

The beam-shape coefficients, a_ℓ^m, depend on the structure of the incident sound wave, which typically is known *a priori*. The scattering coefficients, s_ℓ^m and b_ℓ^m, are obtained by satisfying boundary conditions at the droplet surface,

$$p_\mathrm{I} = p_\mathrm{O} \tag{19a}$$

and

$$\mathbf{u}_\mathrm{I} \cdot \hat{\mathbf{n}} = \mathbf{u}_\mathrm{O} \cdot \hat{\mathbf{n}}. \tag{19b}$$

For a spherical droplet of radius R, which is the simplest case, the scattering coefficients reduce to

$$b_\ell^m = \tilde{\rho} a_\ell^m \left[\frac{j_\ell(kR)}{j_\ell(k_I R)} + s_\ell^m \frac{h_\ell(kR)}{j_\ell(k_I R)} \right] \tag{20a}$$

and

$$s_\ell^m = -\frac{\tilde{\rho}\tilde{c}\, j_\ell(kR)\, j_\ell'(k_\mathrm{I}R) - j_\ell(k_\mathrm{I}R)\, j_\ell'(kR)}{\tilde{\rho}\tilde{c}\, h_\ell(kR)\, j_\ell'(k_\mathrm{I}R) - j_\ell(k_\mathrm{I}R)\, h_\ell'(kR)}, \tag{20b}$$

where $\tilde{\rho} = \rho_\mathrm{O}/\rho_\mathrm{I}$ and $\tilde{c} = k_\mathrm{I}/k = c_\mathrm{O}/c_\mathrm{I}$, and primes denote derivatives with respect to the argument. In the special case $\tilde{c} = 1$, the scattering coefficients simplify further to

$$b_\ell^m = \tilde{\rho} a_\ell^m \left[1 + s_\ell^m \frac{h_\ell(kR)}{j_\ell(kR)} \right] \tag{21a}$$

and

$$s_\ell^m = -\frac{\tilde{\rho} - 1}{\tilde{\rho}\dfrac{h_\ell(kR)}{j_\ell(kR)} - \dfrac{h_\ell'(kR)}{j_\ell'(kR)}}. \tag{21b}$$

Equations (20) and (21) serve as a point of departure for describing scattering by aspherical droplets.

B. Second-order equations for time-averaged dynamics

The first-order incident and scattered sound waves together give rise to steady forces and flows at second order. The steady, time-averaged second-order Navier–Stokes equations,

$$-\nabla \cdot \langle \rho_1 \mathbf{u}_1 \rangle = \rho_0 \langle \nabla \cdot \mathbf{u}_2 \rangle, \tag{22a}$$

$$\langle \rho_1 \partial_t \mathbf{u}_1 + \rho_0 (\mathbf{u}_1 \cdot \nabla)\mathbf{u}_1 \rangle = -\nabla \langle p_2 \rangle + \eta \nabla^2 \langle \mathbf{u}_2 \rangle + \beta\eta \nabla \langle \nabla \cdot \mathbf{u}_2 \rangle, \tag{22b}$$

reduce to

$$-\nabla \langle p_2 \rangle + \eta \nabla \times \langle \nabla \times \mathbf{u}_2 \rangle = \mathbf{f}_R \tag{23}$$

in the limit that that the fluid is incompressible,[31] for which $\langle \nabla \cdot \mathbf{u}_2 \rangle = 0$. The Reynolds stress that drives the flow,

$$\mathbf{f}_R(\mathbf{r}) \equiv \rho_0 \nabla \cdot \langle \mathbf{u}_1 \mathbf{u}_1 \rangle, \tag{24}$$

is obtained from the first-order solution.

The acoustic radiation pressure, $\langle p_2 \rangle$, and vortical acoustic streaming, $\langle \nabla \times \mathbf{u}_2 \rangle$, are given by the irrotational and solenoidal components of $\mathbf{f}_R$, respectively. The latter term vanishes because we neglect viscosity in the first-order fields, which means that $\mathbf{u}_1(\mathbf{r}) = \nabla\phi$ and therefore that the Reynolds stress is irrotational. Consequently, the viscous flows described by the second term on the left-hand side of Eq. (23) vanish. From this, we conclude that the time-averaged radiation pressure is[9,16]

$$\langle p_2 \rangle = \frac{1}{2}\rho_0 \langle u_1^2 \rangle - \frac{1}{2}\frac{1}{\rho_0 c_0^2} \langle p_1^2 \rangle. \tag{25}$$

The second-order pressure wave depends on the squares of the first-order fields and therefore does not vanish on average over the acoustic period. It nevertheless can vary on inertial time scales.

When the boundary layer is thin, $\delta(\omega) \ll R$, Eq. (25) is a good approximation for $\langle p_2 \rangle$ evaluated at the time-averaged position of the droplet surface, and therefore completes the description of the sound wave required to model the acoustic force acting on the droplet through Eq. (10). While we have neglected viscous streaming due to the Reynolds stress, $\mathbf{f}_R(\mathbf{r})$, in Eq. (24), our simulations still have acoustic streaming flows that are driven by the momentum flux advected by the boundary, which is described by the tangential component of Eq. (10). The distinction between these mechanisms is discussed further in Sec. IV D.

C. Acoustic radiation force on a spheroid

Together, Eqs. (10) and (25) express the second-order acoustic radiation force on the droplet in terms of first-order acoustic fields. Analytic solutions for these first-order fields are known for certain geometries with high symmetry. More generally, the scattering coefficients in Eq. (18) may be obtained via a variety of semi-analytic techniques. These include the T-matrix method, which has been extended to acoustics by Waterman,[18] the discrete dipole approximation,[32] and modal-matching methods.[17,33] Here, we introduce an alternative approximation scheme that leverages the exact spherical solution and consequently is more efficient when deformations are small.

To leading order, the fields scattered by a slightly aspherical droplet are approximated by the fields scattered by the minimally enclosing sphere. The simple spherical approximation, however, does not satisfy the appropriate boundary conditions for the fluid velocity at the droplet's surface,

$$[\mathbf{u}_O(\mathbf{r}_s) - \mathbf{u}_I(\mathbf{r}_s)] \cdot \hat{\mathbf{n}}(\mathbf{r}_s) = 0, \tag{26a}$$

$$[\tilde{\rho}\mathbf{u}_O(\mathbf{r}_s) - \mathbf{u}_I(\mathbf{r}_s)] \cdot \hat{\mathbf{t}}(\mathbf{r}_s) = 0, \tag{26b}$$

where $\hat{\mathbf{t}}$ is the surface tangent unit vector, and $\hat{\mathbf{t}} \times \hat{\mathbf{n}} = 0$. The discontinuity in the first-order tangential follows from the assumption that the first-order acoustic fields are inviscid, and accounts for the influence of vortical waves within the viscous boundary layer surrounding the droplet. At second order, these vortical waves exert Reynolds stress on the fluid within the boundary layer, thereby driving viscous streaming in Eq. (23). When the boundary layer is thin, however, this Reynolds stress can be treated as a viscous stress on the droplet's surface that is balanced by tangential radiation stress.[12,15] In this way, the boundary condition in Eq. (26b) preserves the effect of vortical waves on the droplet's time-averaged dynamics while avoiding the need to simulate compressible flows.

Taking $\mathbf{U}(\mathbf{r})$ to be the flow field that would be created by the enclosing sphere, the actual flow field at position $\mathbf{r}_s$ on the surface of the distorted sphere can be approximated by

$$\mathbf{u}_I(\mathbf{r}_s) = \mathbf{U}_I(\mathbf{r}_s), \tag{27a}$$

$$\mathbf{u}_O(\mathbf{r}_s) = \mathbf{U}_O(\mathbf{r}_s) + \boldsymbol{\delta}(\mathbf{r}_s). \tag{27b}$$

This flow field satisfies the boundary conditions in Eq. (26) if

$$\boldsymbol{\delta}(\mathbf{r}_s)\cdot\hat{\mathbf{r}} = n_\theta(\mathbf{r}_s)\left(1-\frac{1}{\tilde{\rho}}\right)\mathbf{U}_I(\mathbf{r}_s)\cdot\hat{\mathbf{t}}(\mathbf{r}_s), \tag{28a}$$

and

$$\boldsymbol{\delta}(\mathbf{r}_s)\cdot\hat{\theta} = n_\theta(\mathbf{r}_s)\left(1-\frac{1}{\tilde{\rho}}\right)\mathbf{U}_I(\mathbf{r}_s)\cdot\hat{\mathbf{n}}(\mathbf{r}_s), \tag{28b}$$

where $\hat{\mathbf{r}}$ and $\hat{\theta}$ are the radial and polar unit vectors in spherical coordinates, respectively, and $n_\theta \equiv \hat{\mathbf{n}}(\mathbf{r}_s)\cdot\hat{\theta}$

The velocity field obtained with Eq. (28) does not necessarily satisfy the Helmholtz equation, nor is it necessarily curl-free. Both of these conditions are *approximately* satisfied, however, so long as the droplet's distortions are small, $n_\theta \ll 1$. Moreover, $\mathbf{u}(\mathbf{r})$ satisfies the boundary conditions from Eq. (19), and therefore should accurately represent the induced flow near the droplet's surface. The efficacy of this approximation scheme is demonstrated in Sec. IV.

Streaming flows generated by a droplet's response to acoustic radiation forces are typically several orders of magnitude slower than the speed of sound in the medium. We therefore ignore any influence of streaming flows on the sound waves that drive them.

D. Computational cost analysis and range of applicability

Numerically resolving a sound wave's propagation requires time steps that are substantially smaller than the acoustic period. Our approach eliminates the need to resolve such short-time processes by relying instead on analytic expressions for first-order scattering. We therefore can resolve time-averaged droplet dynamics and streaming flows with time steps that span multiple acoustic periods. The difference between dynamical and acoustic time scales therefore represents the computational cost savings of the hybrid IB method. When applied to a micrometer-scale droplet moving through water under the influence of megahertz-scale ultrasound, the number of flow-field evaluations is reduced at least 1000-fold. This estimate is discussed in detail in Appendix D.

Comparison with existing high-order acoustic IB schemes show that these savings are realized in practice. The acoustic IB method presented in Ref. 8, for example, computes the influence of acoustic forces on a micrometer-sized red blood cell by directly solving the compressible Navier–Stokes equations using a 5th-order Weighted Essentially Non Oscillatory (WENO) scheme. The WENO scheme numerically resolves acoustic wave propagation with time step $dt \approx R/c \approx 1.33$ ns. By treating acoustic-scale processes semi-analytically, the hybrid IB method can model time-averaged acoustic stresses on a micrometer-scale droplet with time steps of 15 μs, which represents a ten-thousand-fold improvement in efficiency.

Realizing these cost savings, however, requires analytic expressions for the first-order acoustic fields scattered by the surface of the droplet. The scattering approximation used in our simulation framework is exact for spherical droplets and also accommodates moderately deformed droplets close to the nodal plane. Large deformations or large displacements from the node require more costly semi-analytical techniques.[17,18,32,33] In this case, a more detailed cost analysis is required to determine whether the hybrid IB method is a suitable alternative to traditional compressible flow solvers.

IV. RESULTS: DROPLET IN A STANDING PLANE WAVE

Section II introduces an IB method that models the dynamics of a droplet suspended in a fluid under the general influence of external forces. Section III explains how sound propagating through the fluid generates such forces. Purely analytic solutions to the sound-driven moving-boundary problem are not yet available. Any purely numerical description of the sound wave[34,35] would have to iterate through an enormous range of time scales to capture the moving droplet's steady dynamics. Our hybrid implementation describes the sound wave semi-analytically and handles the moving-boundary problem numerically. The result is an accurate and exceptionally efficient implementation.

We demonstrate the efficacy of the hybrid IB method with an illustrative model system: a single droplet levitated in a planar acoustic standing wave, as shown schematically in Fig. 4. To set up the IB method for this system, we specify the standing wave's scalar potential,

$$\phi_i(\mathbf{r}) = \phi_0 \sin(kz), \tag{29}$$

with amplitude ϕ_0 and a nodal plane at $z = 0$. The associated beam-shape coefficients,[6]

$$a_\ell^m = (2\ell+1)\cos\left(kz + \frac{\ell\pi}{2}\right). \tag{30}$$

yield a compact expression for the net ARF on the droplet:

$$\sum_{i=0}^{N_b}\mathbf{F}_i^{ARF} = \frac{1}{2}\rho_0\phi_0^2\,Q\,\sin(2kz)\,\hat{z}, \tag{31}$$

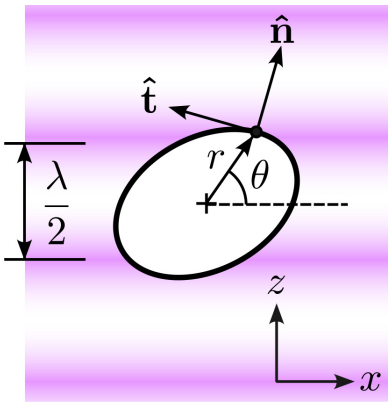

FIG. 4. A spheroidal droplet in a plane standing wave. Antinodes of the pressure wave are separated by half the acoustic wavelength in the medium, λ. The droplet's shape, $r(\theta)$, is specified in polar coordinates relative to its center. Boundary conditions are applied in the normal, $\hat{\mathbf{n}}(\theta)$, and tangential, $\hat{\mathbf{t}}(\theta)$, directions relative to the droplet's surface.

where the radiation force efficiency, Q, is a dimensionless scattering coefficient that depends on droplet geometry and boundary conditions.[5,6] For a rigid sphere in a standing wave, $Q = k^3 V_p/5$, where V_p is the volume of the particle.[6] The scale of the acoustic force, $\frac{1}{2}\rho_0\phi_0^2$, is set by the driving voltage in experimental realizations.[5]

The simulations described in this section are all performed on a $50 \times 50\,\mu\text{m}^2$ periodic domain that is discretized on a 256 pixel $\times$ 256 pixel grid. The droplet's boundary is modeled with 100 boundary markers, and its excess density is modeled by 150 mass-marker pairs. Iterations are performed with a time step of 15 μs until a final time of about 6 s.

Each simulation starts with a spherical droplet of radius $R = 2\,\mu$m and density $\rho_I = 1.18\,\text{g cm}^{-3}$, dispersed in water. The droplet is subject to a buoyant force, $F_g = (\rho_I - \rho_0)\,V_p g \approx 60$ pN, that is balanced by acoustic forces. To model practical acoustic levitators for water-borne samples,[5] the driving frequency is set to 2 MHz. The dimensionless size parameter, $kR = 0.034$, is well within the Rayleigh limit, $kR \ll 1$. The droplet initially is released at the nodal plane and then relaxes to its equilibrium position, z_0, and to its equilibrium shape.

A. Comparison to analytic solution for a spheroid

We test the approximation scheme from Sec. III C by considering the special case of spheroidal droplets, whose scattering coefficients can be expressed analytically in spheroidal coordinates.[30] The associated spheroidal wave functions are much more costly to evaluate than spherical harmonics, which limits the utility of the analytic solution for time-resolved simulations. Analytic solutions for spheroids are useful, nonetheless, for validating our computationally efficient approximation scheme.

Figure 5 compares analytic and approximate force profiles computed for spheroids of various eccentricities. Each spheroid is taken to be displaced by $z_0 = -0.15\mu$m from the node of a standing wave, characterized by the beam-shape coefficients. Equation (30). The "spherical" approximation, plotted in blue, is obtained by plugging $\mathbf{u}_1 = \mathbf{u}_O(\mathbf{r}_s) \approx \mathbf{U}_O(\mathbf{r}_s)$ into Eq. (10). Likewise, the "corrected" approximation, plotted in orange, is obtained by plugging $\mathbf{u}_1 = \mathbf{u}_O(\mathbf{r}_S) \approx \mathbf{U}_O(\mathbf{r}_s) + \boldsymbol{\delta}(\mathbf{r}_s)$ from Eqs. (27) and (28) into Eq. (10). Both are compared to the exact solution resulting from solving the scattering problem analytically in spheroidal coordinates, which is plotted in green.

The spherical approximation has qualitatively different behavior from the exact solution even at small deformations. By contrast, the corrected approximation agrees with the exact solution for moderate deformations. The normal component of the computed force tracks the functional form of the exact solution up to a reasonably small multiplicative factor. This discrepancy should not significantly affect the shape or dynamics of the droplet, which is assumed to be incompressible. Agreement with the analytic solution is much better for the tangential forces, which are responsible for driving acoustic streaming flows in our simulations. The hybrid IB method therefore should predict the structure of streaming flows far more accurately than the simple spherical approximation, and far more efficiently than the analytic solution. A further discussion of limitations of Eq. (28) is provided in Appendix C.

B. Parameters of interest

In the long wavelength limit, $kR \ll 1$, the first-order fields are dominated by the monopole ($\ell = 0$) and dipole ($\ell = 1$) terms of Eq. (18), which describe pulsation and translation modes, respectively. The acoustic radiation force from Eq. (10), being quadratic in the

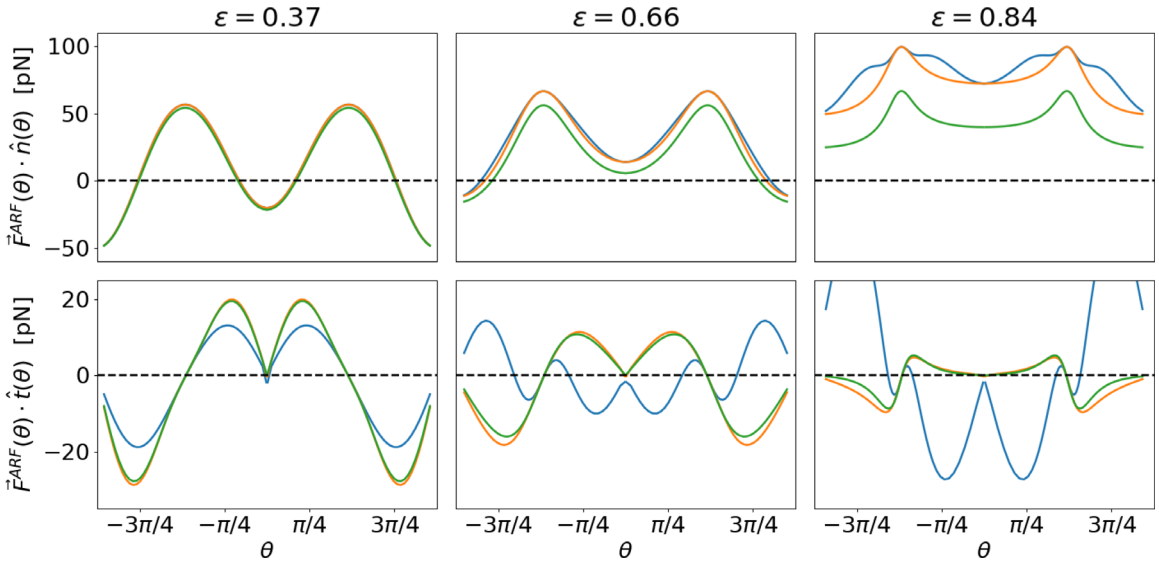

FIG. 5. Normal and tangential components of the acoustic radiation force at the surface of a droplet that is displaced from the nodal plane of a standing plane wave by $z_0 = -0.15\,\mu$m. Exact results for spheroidal droplets[30] are plotted in green and are compared with predictions of Eq. (21) for the equivalent sphere (blue) and with the projected forces from Eq. (26) (orange). Deviations from the exact interfacial force increase as the droplet's ellipticity increases from $\varepsilon = 0.37$ to 0.84. The tangential component of the projected force, however, closely tracks the exact profile even at the largest ellipticity, which means that the hybrid IB method should reliably predict the droplet's shape and streaming flows when displacements from the node are not too large.

first-order fields, is dominated by monopole–monopole (00), monopole–dipole (01), and dipole–dipole (11) products of the first-order fields. The (00) mode has no angular dependence and therefore constitutes an acoustic correction to hydrostatic pressure. The acoustic force on the droplet, therefore, is dominated by a superposition of (01) and (11) modes.

The (01) and (11) modes are linear and quadratic in $\cos\theta$ and its derivatives, respectively. As a direct consequence of this angular dependence, the normal component of the (01) mode exerts a net radiation force that affects the droplet's position, whereas the normal component of the (11) mode affects the droplet's shape. Likewise, the tangential component of the (01) mode drives dipole streaming flows around the droplet, whereas the (11) mode drives quadrupole streaming flows.

To investigate this behavior, we perform hybrid IB method simulations over a range of values of trap strength, ϕ_0^2, and surface tension, σ. The trap strength controls the droplet's equilibrium position, which affects the relative strength of pulsational and translational modes according to the beam-shape coefficients from Eq. (30). Consequently, varying trap strength alone is sufficient to probe the entire range of accessible acoustic forces between (01)-dominated and (11)-dominated modes. Surface tension controls the droplet's shape, allowing us to study droplet deformation and shape-dependent acoustic driving.

C. Equilibrium shape of a levitated droplet

The equilibrium shape of a droplet in an acoustic field is typically found analytically by relating the surface curvature to acoustic stresses with the Young–Laplace formula.[36,37] Working in two dimensions, the equilibrium shape of a slightly deformed droplet of radius R may be expanded in associated Legendre polynomials,[15]

$$r(\theta) = R + \sum_{\ell=0}^{\infty} \sum_{m=-\ell}^{\ell} x_{\ell m} P_\ell^m(\cos\theta). \tag{32}$$

When the droplet has the same viscosity as the medium, the normal force, $F_n(\theta) = \mathbf{F}^{ARF} \cdot \hat{\mathbf{n}}$, determines the static shape deformation,[15,38]

$$x_{\ell m} = \frac{R^2}{(\ell+2)(\ell-1)\,\sigma} \int_{-1}^{1} F_n(\theta)\, P_\ell^m(\cos\theta)\, d\cos\theta. \tag{33}$$

In a standing wave, the primary deformation mode is described by x_{20}, which flattens the droplet into a roughly elliptical shape. Figure 6 compares the value of x_{20} observed in IB method simulations of a droplet of $R = 2\,\mu$m with predictions of Eq. (33) over a range of values of surface tension, σ, and trap strength, ϕ_0^2. The computed deformation agrees well for droplets close to the trapping plane, and deviates at larger displacements from the node. This is because our approximation for scattering, Sec. III C, begins to break down at larger displacements from the node.

D. Acoustic streaming

Acoustic forces not only translate and deform the droplet, but also generate interior and exterior streaming flows. The streaming profiles for an acoustically levitated fluid droplet are characterized by a transition from dipolar flow to quadrupolar flow depending on the relative magnitude of acoustically driven pulsation and translation modes, respectively.[14] The streaming behavior depends on scattering properties of the droplet, as well as the local structure of the incident acoustic wave.

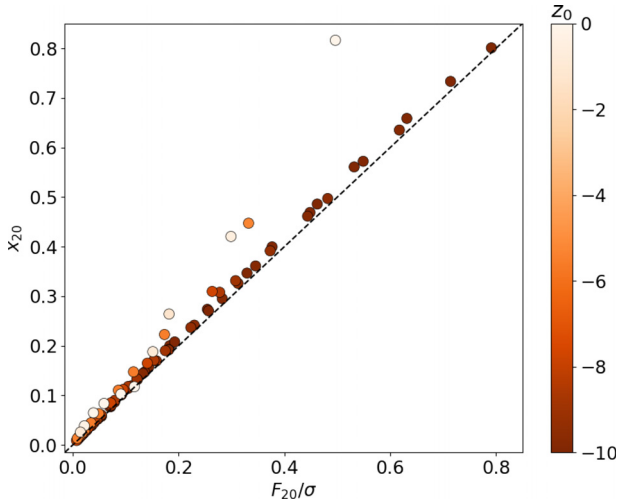

FIG. 6. Dependence of a droplet's degree of deformation on the relative strength of the acoustic driving. Outliers represent droplets that were not stably trapped.

1. Spherical droplets

The streaming profiles around a spherical fluid droplet in an acoustic levitator have been computed analytically by Baasch *et al.*[14] Their solution should be comparable to results of the hybrid IB method under conditions where shape deformations are small, i.e., $\sigma R \gg \rho_0 \phi_0^2$. The results in Fig. 7 are obtained by fixing the surface tension at a fairly large value, $\sigma = 3.3\,\text{nN}\,\mu\text{m}^{-1}$, and varying the trap strength, ϕ_0^2. Because the droplet is more dense than its medium, it sinks below the nodal plane by a distance that is inversely proportional to the traps' strength and therefore samples different regions of the acoustic force landscape. This has consequences for the nature of the induced streaming flow.

Figure 7(a) shows the quadrupolar streaming flow that is induced when the droplet is far below the nodal plane in a comparatively weak acoustic trap. Increasing ϕ_0 by a factor of 3 in Fig. 7(b) lifts the droplet toward the nodal plane and qualitatively transforms the streaming flow into a principally dipolar motif. This transition from quadrupolar to dipolar flow with increasing trap stiffness has been predicted analytically and is reported in Fig. 7 of Ref. 14. The computed streamlines in Figs. 7(a) and 7(b) agree well with the analytic results from Ref. 14. Further increasing the trap stiffness in Fig. 7(c) lifts the particle still closer to the nodal plane and induces a second transition back to quadrupolar streaming. This second transition appears not to have been reported previously.

2. Mechanisms for spherical streaming

The streaming flows in our simulations are driven entirely by the tangential component of the acoustic radiation force at the droplet's surface. By contrast, the streaming observed in Ref. 14 arises entirely from first-order vorticity, which we neglect. Our results suggest that these two distinct mechanisms drive the same type of streaming near

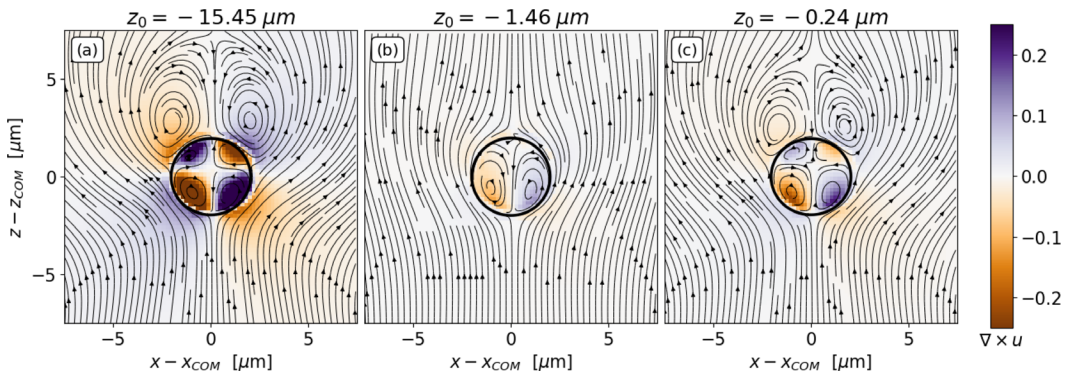

FIG. 7. Streaming profiles for a droplet levitated in water with $\sigma = 3.3\,\text{nN}\,\mu\text{m}^{-1}$ and $R = 2\,\mu\text{m}$ at various trap strengths. (a) Gravity displaces the droplet downward from the nodal plane, favoring quadrupolar streaming in the weakest levitator. (b) Increasing trap strength induces a crossover to dipolar streaming. (c) Increasing trap strength further induces a second crossover to quadrupolar flow. The flow's vorticity is indicated by color.

the surface of a fluid droplet. Qualitatively, this occurs because tangential radiation stresses are balanced by tangential viscous stresses at the fluid–fluid interface.[15] When viewed in this light, agreement between our simulations and Ref. 14 is expected because streaming profiles in both frameworks are governed by the relative strength of (01) and (11) modes.[14]

Figure 8 illustrates the relationship between the tangential ARF, $\mathbf{F}_\theta(\theta) = \mathbf{F}^{ARF}(\theta) \cdot \hat{\theta}$, and the vortex structure of the resulting streaming flows. Figure 8(a) presents the normalized tangential ARF,

$$\tilde{F}_\theta(\theta) = \frac{F_\theta(\theta)}{\max\{|F_\theta(\theta)|\}} \tag{34}$$

as a function of position, θ, on the droplet's surface. Normalizing in this way emphasizes the relative strengths with which the upper and lower vortices are driven. The maximum of this quantity,

$$\mathscr{Q} = \max\{\tilde{F}_\theta(\theta)\} \tag{35}$$

is a convenient metric for the degree of quadrupolar vs dipolar flow. When $\mathscr{Q} = 1$, the upper and lower vortices are driven with equal vigor, leading to quadrupolar flow. By contrast, $\mathscr{Q} = 0$ describes dipolar flow.

Figure 8(b) tracks the reentrant transition between quadrupolar and dipolar flow as a function of trap strength, as monitored by the droplet's equilibrium position, z_0. Scaling z_0 by the droplet radius, R, effectively collapses $\mathscr{Q}(z_0)$ onto a master curve. In all cases, the flow is observed to be purely dipolar when $z_0 = z_0^* \approx 0.92R$. Figure 8(c) illustrates the dependence of z_0^* on the density of the droplet.

The analysis from Fig. 8 uses the exact analytic form of the acoustic radiation force on a sphere to predict the dependence of acoustic driving on a variety of parameters. In Sec. IV D 3, we consider the case of an aspherical droplet. Because the expression for the acoustic radiation force on an ellipse is difficult to manipulate analytically, our simulations offer insights into the relationship between droplet shape and acoustic streaming that would be difficult to obtain by other means.

3. Deformable droplets

Both dynamical transitions reported in Fig. 7 occur for droplets that are stiff enough to remain substantially spherical while trapped.

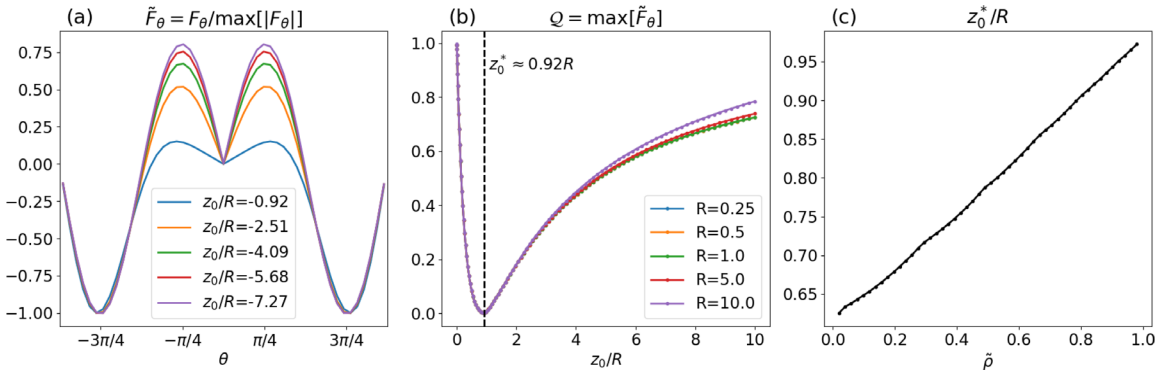

FIG. 8. (a) Variation of the normalized tangential ARF, $\tilde{F}_\theta(\theta)$, as a function of position, θ, on the droplet's surface for different values of the droplet's equilibrium position, z_0. The four extrema drive four vortexes in the streaming flow. Suppressing the two maxima favors dipolar streaming. (b) Dependence of the maxima, $Q = \max\{\tilde{F}_\theta(\theta)\}$, on trap strength, as monitored by displacement z_0. Results for different droplet radii, R, collapse onto a master curve when z_0 is scaled by R. Quadrupolar flows are favored at both high and low trap strength. Dipolar flows are favored when $z_0 = z_0* = 0.92R$. (c) Dependence of z_0^*/R on the droplet's density, ρ_I relative to that of the medium, ρ_O through $\tilde{\rho} = \rho_O/\rho_I$. A density-matched droplet, $\tilde{\rho} \approx 1$, has $z_0^* \approx R$.

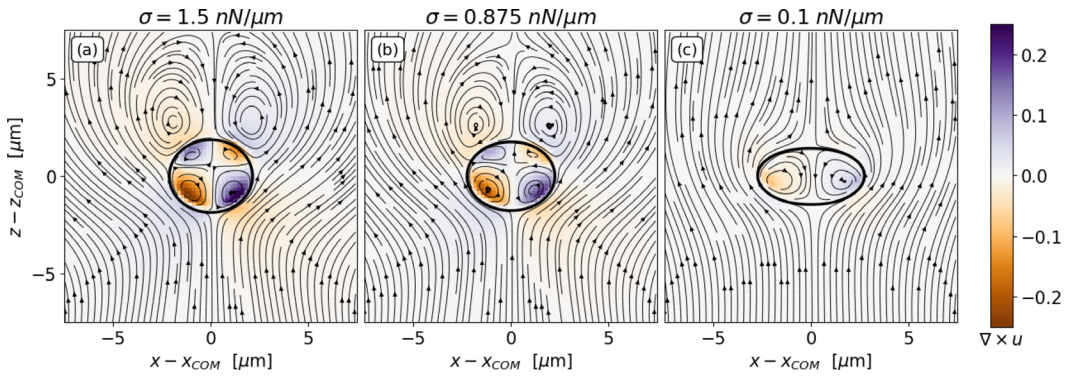

FIG. 9. Streamlines of the streaming flow for a droplet of radius $R = 2\,\mu$m in a strong levitator, $z_0 \approx -0.15\,\mu$m, simulated under the conditions considered in Fig. 5. (a) Reducing the surface tension, σ, by half relative to Fig. 7 allows the droplet to deform while retaining quadrupolar flows. (b) Further reducing surface tension increases the droplet's distortion while significantly decreasing the vorticity in the streaming flow. (c) A highly deformable droplet induces dipolar streaming flows.

This is consistent with the assumption of sphericity that underlies the analysis in Ref. 14. Figure 9 reveals yet another dynamical transition that occurs when a strongly trapped droplet is soft enough to deform, a scenario that has not been considered in previous studies. The droplet in Fig. 9(a) is comparable to the droplet in Fig. 7(c), except that its surface tension is smaller by a factor of two. The droplet consequently deforms into a spheroid under the uniaxial stress of the acoustic levitator and settles at a slightly different height relative to the nodal plane. The induced streaming flow nevertheless retains its quadrupolar nature.

Reducing the surface tension, in Fig. 9(b), increases the distortion and moves both the interior and exterior circulation closer to the droplet surface. Reducing the surface tension still further, in Fig. 9(c), suppresses the vortex structure entirely. The streaming flow around the spheroidal droplet is primarily dipolar. This deformation-induced dynamical transition also appears not to have been observed in prior studies. These observations illustrate the value of the hybrid IB method for probing the dynamical properties of insonated droplets.

V. DISCUSSION

We have introduced a hybrid immersed boundary method that efficiently models the stresses on acoustically levitated droplets and the surrounding fluid. We have validated our method by simulating a single droplet in a plane standing wave, and comparing the results with the best available analytical and numerical solutions. Even in this minimal system, the hybrid IB method reveals transitions between dipolar and quadrupolar streaming under strong-driving conditions that have not been reported in previous studies. These observations offer insights into the response of deformable droplets to the forces and torques created by acoustic landscapes.

Compared to traditional compressible flow simulations, our hybrid method cuts computational cost by utilizing semi-analytic techniques to incorporate acoustic scattering in to hydrodynamic simulations. The benefits are greatest when stress-induced deformations are small enough that analytic scattering calculations can be carried out rapidly. When the droplet shape is highly irregular and unpredictable, most known semi-analytic techniques converge slowly and may be prohibitively expensive. However, for droplets with small to moderate deformations, the hybrid IB method may be up to four orders of magnitude faster than compressible flow simulations. For the implementation presented here, the hybrid method efficiently and effectively models spheroidal shape deformations and streaming profiles around a single droplet, and can easily be scaled up to study acoustohydrodynamic interactions among multiple particles.

Our hybrid IB method employs a two-dimensional model to study the dynamics of acoustically trapped droplets in real three-dimensional experiments. This simplification trades generality for computational efficiency and consistency with analytic formulations of similar systems. For single droplet levitation, which is generally characterized by axial symmetry,[14,33,39] our two-dimensional simulation is both more efficient and offers more direct comparison to two-dimensional expressions in the literature. However, there are many cases for which these symmetries might be broken in a fully three-dimensional treatment,[40] including asymmetric acoustic fields, asymmetric droplet deformations, or certain multiple-particle systems.[5] Fortunately, the hybrid IB method may be readily to three-dimension by replacing the associated Legendre polynomials in Eq. (18) with spherical harmonics, and reformulating surface tension for a three-dimensional surface. Generalizing the hybrid IB method to three dimensions[41] still would offer substantial benefits relative to fully computational methods.

The streaming flows generated by acoustic wave-matter interactions are fundamentally different from those due to external flows around an obstacle because the former are driven by local stresses at the droplet's boundary. These acoustic stresses follow directly from the momentum transferred to the droplet by acoustic scattering. Because first-order sound waves vanish from time-averaged dynamics, their action on the droplet is analogous to that of active particles on their surroundings by internal energy consumption. The resulting streaming flows, in turn, may lead to acoustically driven hydrodynamic coupling in multi-particle systems, which might mediate anomalous collective phenomena observed in experimental studies of acoustically levitated droplets.[5]

The framework presented here is extremely flexible. The hybrid IB method can be extended to accommodate large shape deformations by incorporating more advanced formulations of acoustic scattering. It can account for viscous streaming in the boundary layer around a droplet by incorporating viscous waves from Eq. (13b). Pairwise forces, like the Bjerknes force,[5] may also be incorporated in Eq. (11). Or, as in

this work, inexpensive approximations can be used throughout to efficiently model qualitative behaviors.

ACKNOWLEDGMENTS

This work was supported by the National Science Foundation under Award No. DMR-2104837.

We are grateful to Professor Charles Peskin for extensive discussions on the formulation of the immersed boundary Method.

AUTHOR DECLARATIONS

Conflict of Interest

The authors have no conflicts to disclose.

Author Contributions

Jacqueline B. Sustiel: Conceptualization (equal); Investigation (lead); Methodology (lead); Software (lead); Validation (lead); Visualization (lead); Writing – original draft (lead); Writing – review & editing (equal). **David G. Grier:** Conceptualization (equal); Funding acquisition (lead); Methodology (supporting); Project administration (lead); Resources (lead); Software (equal); Supervision (lead); Validation (supporting); Visualization (equal); Writing – original draft (equal); Writing – review & editing (equal).

DATA AVAILABILITY

The data that support the findings of this study are available from the corresponding author upon reasonable request.

APPENDIX A: SPATIOTEMPORAL DISCRETIZATION OF THE IB METHOD

Our implementation of the IB method uses a staggered marker-and-cell (MAC) spatial discretization scheme described in Refs. 24 and 42. In this implementation, the components α of the flow field, $u_\alpha(\mathbf{x}_j + \hat{\alpha}h)$ are discretized on a grid that is staggered with respect to the scalar fields, $p(\mathbf{x}_j)$ and $\rho(\mathbf{x}_j)$, as illustrated by Fig. 2.1 of Ref. 24. Finite difference, averaging, skew, and Laplacian operators are discretized as[24]

$$(D_\alpha\phi)(\mathbf{x}) = \frac{\phi(\mathbf{x}+\hat{\alpha}\mathbf{h}) - \phi(\mathbf{x}-\hat{\alpha}\mathbf{h})}{h}, \tag{A1}$$

$$(A_\alpha\phi)(\mathbf{x}) = \frac{\phi(\mathbf{x}+\hat{\alpha}\mathbf{h}) + \phi(\mathbf{x}-\hat{\alpha}\mathbf{h})}{h}, \tag{A2}$$

$$S(\mathbf{u})v_\alpha = \frac{1}{2}\sum_\beta \left[A_\beta\big((A_\alpha u_\beta)(D_\beta v_\alpha)\big) + D_\beta\big((A_\alpha u_\beta)(A_\beta v_\alpha)\big)\right], \tag{A3}$$

$$(L(\mu)\mathbf{u})_\alpha = \sum_\beta D_\beta(\mu(\mathbf{x}_j)(D_\alpha u_\beta + D_\beta u_\alpha), \tag{A4}$$

respectively.

Reference 24 uses a seven-point discrete delta function and predictor-corrector temporal scheme to accommodate variable density and viscosity. However, the staggered MAC scheme is itself sufficient to dramatically improve the volume conservation properties of the standard IB method. With this in mind, we opt to use the four-point delta function and temporal discretization scheme described in Sec. 6 and 7 of Ref. 20. The discrete delta function is

$$\delta_h(\mathbf{x}) = \frac{1}{h^2}\,\phi\left(\frac{x}{h}\right)\phi\left(\frac{x}{h}\right), \tag{A5a}$$

where

$$\phi(r) = \frac{1}{8}\begin{cases} 0, & r \le 2, \\ 5 + 2r - \sqrt{-7 - 12r - 4r^2}, & -2 \le r \le -1, \\ 3 + 2r + \sqrt{1 - 4r - 4r^2}, & -1 \le r \le 0, \\ 3 - 2r + \sqrt{1 + 4r - 4r^2}, & 0 \le r \le 1, \\ 5 - 2r - \sqrt{-7 + 12r - 4r^2}, & 1 \le r \le 2, \\ 0, & 2 \le r. \end{cases} \tag{A5b}$$

The temporal discretization is a second-order accurate Runge–Kutta method based on the midpoint rule, identical to Sec. 7 of Ref. 20 except with differential operators replaced by those from the MAC scheme.

APPENDIX B: FLOWS AROUND A SEDIMENTING SPHERICAL DROPLET

Analytic solutions are available for the viscous flow fields inside and around a spherical fluid droplet as it moves with velocity $\mathbf{v} = v\hat{z}$ through an immiscible fluid.[26] Assuming that the two fluids have the same viscosity, the stream functions inside and outside the droplet are

$$\psi^{(i)}(\mathbf{r}) = \frac{1}{8}v r^2\left(\frac{r^2}{a_p^2} - 1\right)\sin^2\theta, \tag{B1}$$

and

$$\psi^{(o)}(\mathbf{r}) = \frac{1}{8}v\frac{a_p^3}{r}\left(1 - 5\frac{r^2}{a_p^2}\right)\sin^2\theta, \tag{B2}$$

respectively. The associated flow field is

$$\mathbf{u}(\mathbf{r}) = \nabla \times (\psi\hat{z}). \tag{B3}$$

APPENDIX C: APPLICABILITY OF THE SCATTERING APPROXIMATION FROM SEC. III C

The approximation in Sec. III C is derived by assuming that the acoustic fields at the droplet surface, $r = S(\theta)$, are similar to that at a minimally enclosing sphere, $r = R \equiv \max[S(\theta)]$. The interior potential from Eq. (18a) can be rewritten by Taylor expanding the radial function to first order in $S - R$,

$$j_\ell(kS) = j_\ell(k_\mathrm{I}R) + (S - R)kj'_\ell(k_\mathrm{I}R) + \mathcal{O}\{(S-R)^2\}.$$

In the long-wavelength limit, $kR \ll 1$, we can use the small-argument asymptotic form $j_\ell(z) \propto x^\ell$, which yields

$$j_\ell(kS) = \left[1 + \ell\left(\frac{S}{R} - 1\right)\right] j_\ell(k_I R) + \mathcal{O}\{(S-R)^2\}$$

so that $\phi_I(R) \approx \phi_I(S)$ as long as

$$\left(\frac{S}{R} - 1\right) \ll \frac{1}{\ell}$$

for all non-negligible modes. Likewise, repeating this procedure for the scattered field reveals that $\phi_s(R) \approx \phi_s(S)$ when $\left(\frac{S}{R} - 1\right) \ll 1/(\ell+1)$.

Because the error in the radial function is proportional to ℓ, higher modes are approximated more accurately than lower modes. Consequently, the applicability of this method also depends on the local structure of the acoustic field. In this work, we have shown in Fig. 5 that our approximation performs well when the droplet is close to the node, even at moderately large deformations. However, as illustrated by Fig. 10, the range of validity is restricted to smaller deformations when the droplet is further from the node.

APPENDIX D: ACOUSTIC AND INERTIAL TIMESCALES

The system considered in this study consists of micrometer-scale fluid droplets levitated in water by a megahertz-range sound wave. Resolving the fields in each cycle of the acoustic wave would require a computational time step much smaller than 1 μs: $dt \approx 10^{-8}$ s for 100-fold sampling. By contrast, the droplet deforms

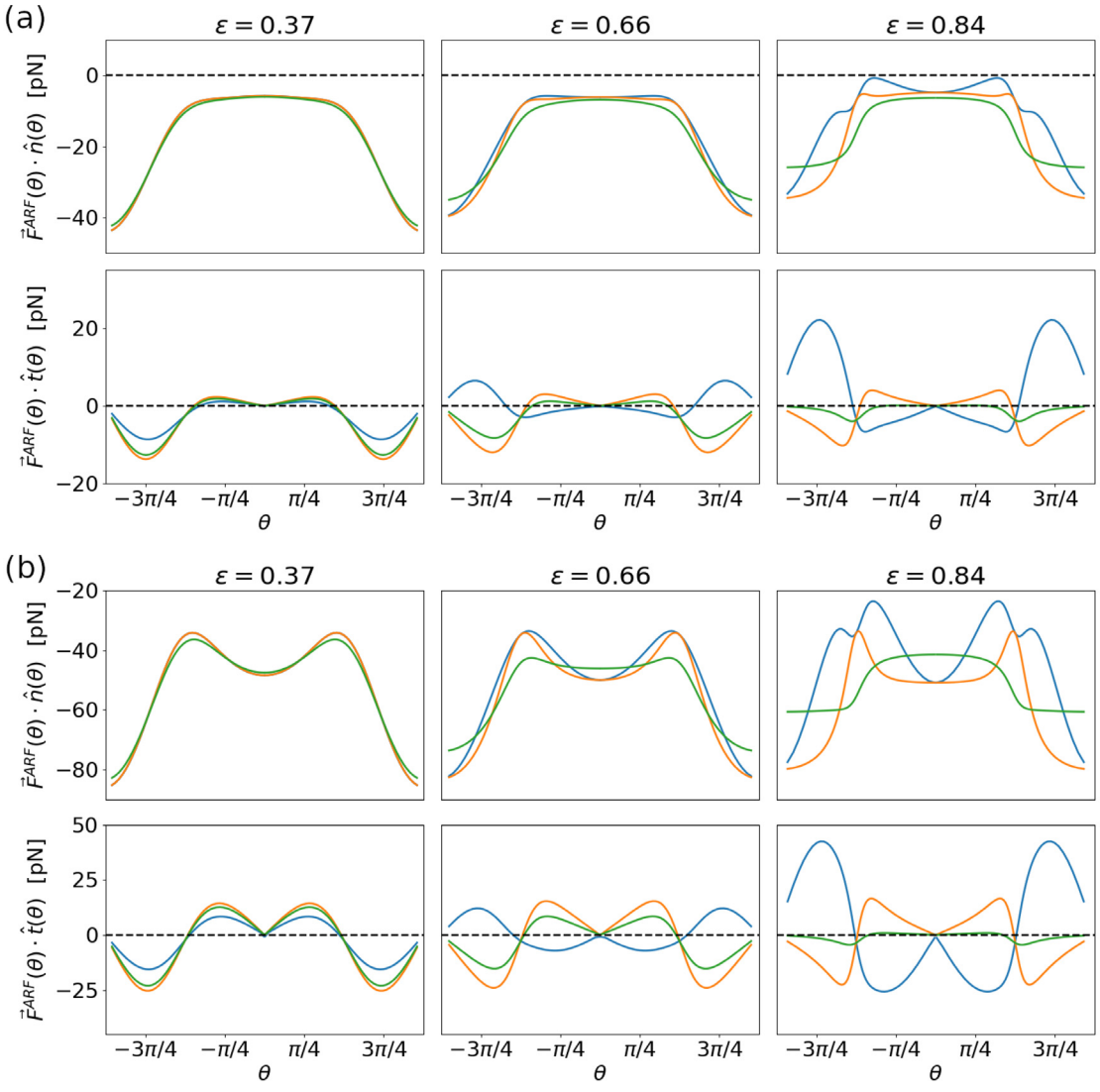

FIG. 10. Normal and tangential components of the acoustic radiation force as a function of position, θ, on the droplet surface for spheroids of various eccentricities: (a) moderate displacement: $z_0 = -3.5$ μm and (b) larger displacement: $z_0 = -10.6$ μm. The ARF at the surface is calculated using the spherical fields from Eq. (21) (blue), the projection correction described in Eq. (26) (orange), and the exact analytic solution in spheroidal coordinates (green).

on a timescale set by external forces, which are all roughly commensurate with gravity. The droplet's terminal free fall velocity through the medium therefore gives a reasonable upper limit for the timescale at which time-averaged deformations occur. Equating the force of gravity, $F_g \approx 60$ pN, to the Stokes drag on a sphere, $F_d = 6\pi R\eta u$, yields a terminal velocity of $u \approx 2\,\mu\text{m s}^{-1}$. To properly sample the translation and deformation of the boundary, we impose the condition that the boundary not moves a distance larger than $R/100$ in a single time step. The time step required to resolve the droplet's motion is therefore $(0.02\,\mu\text{m})/(2\,\mu\text{m s}^{-1}) \approx 10$ ms.

The 15 μs time step used in our simulation is much finer than needed to resolve the droplet's dynamics and is chosen to ensure stability of the penalty IB method described in Sec. II B. In practice, this requirement might be addressed by relaxing the tolerance of the penalty IB method or by employing other multiphase flow schemes.[24] Such an enhancement could realize a few more orders of magnitude in cost savings.

REFERENCES

[1]S. Santesson and S. Nilsson, "Airborne chemistry: Acoustic levitation in chemical analysis," Anal. Bioanal. Chem. **378**, 1704–1709 (2004).
[2]M. A. Andrade, N. Pérez, and J. C. Adamowski, "Review of progress in acoustic levitation," Braz. J. Phys. **48**, 190–213 (2018).
[3]C. Mu, J. Wang, K. M. Barraza, X. Zhang, and J. L. Beauchamp, "Mass spectrometric study of acoustically levitated droplets illuminates molecular-level mechanism of photodynamic therapy for cancer involving lipid oxidation," Angew. Chem. Int. Ed. **58**, 8082–8086 (2019).
[4]A. Marzo and B. W. Drinkwater, "Holographic acoustic tweezers," Proc. Natl. Acad. Sci. U. S. A. **116**, 84–89 (2019).
[5]M. A. Abdelaziz, J.-L. Aider, D. J. Pine, D. G. Grier, M. Hoyos *et al.*, "Ultrasonic chaining of emulsion droplets," Phys. Rev. Res. **3**, 043157 (2021).
[6]G. T. Silva and B. W. Drinkwater, "Acoustic radiation force exerted on a small spheroidal rigid particle by a beam of arbitrary wavefront: Examples of traveling and standing plane waves," J. Acoust. Soc. Am. **144**, EL453–EL459 (2018).
[7]J. T. Karlsen and H. Bruus, "Forces acting on a small particle in an acoustical field in a thermoviscous fluid," Phys. Rev. E **92**, 043010 (2015).
[8]L. Wang, F.-B. Tian, and J. C. Lai, "An immersed boundary method for fluid–structure–acoustics interactions involving large deformations and complex geometries," J. Fluids Struct. **95**, 102993 (2020).
[9]H. Bruus, "Acoustofluidics 7: The acoustic radiation force on small particles," Lab Chip **12**, 1014–1021 (2012a).
[10]W. L. Nyborg, "Acoustic streaming near a boundary," J. Acoust. Soc. Am. **30**, 329–339 (1958).
[11]Q. Qi, "The effect of compressibility on acoustic streaming near a rigid boundary for a plane traveling wave," J. Acoust. Soc. Am. **94**, 1090–1098 (1993).
[12]C. P. Lee and T. G. Wang, "Outer acoustic streaming," J. Acoust. Soc. Am. **88**, 2367–2375 (1990).
[13]P. J. Westervelt, "The theory of steady rotational flow generated by a sound field," J. Acoust. Soc. Am. **25**, 60–67 (1953).
[14]T. Baasch, A. A. Doinikov, and J. Dual, "Acoustic streaming outside and inside a fluid particle undergoing monopole and dipole oscillations," Phys. Rev. E **101**, 013108 (2020).
[15]P. L. Marston, "Shape oscillation and static deformation of drops and bubbles driven by modulated radiation stresses—theory," J. Acoust. Soc. Am. **67**, 15–26 (1980).
[16]H. Bruus, "Acoustofluidics 2: Perturbation theory and ultrasound resonance modes," Lab Chip **12**, 20–28 (2012b).
[17]F. Mitri, "Axial acoustic radiation force on rigid oblate and prolate spheroids in bessel vortex beams of progressive, standing and quasi-standing waves," Ultrasonics **74**, 62–71 (2017).
[18]P. Waterman, "T-matrix methods in acoustic scattering," J. Acoust. Soc. Am. **125**, 42–51 (2009).
[19]C. S. Peskin, "Flow patterns around heart valves: A numerical method," J. Comput. Phys. **10**, 252–271 (1972).
[20]C. S. Peskin, "The immersed boundary method," Acta Numer. **11**, 479–517 (2002).
[21]S. Maramizonouz, M. Rahmati, A. Link, T. Franke, and Y. Fu, "Numerical and experimental studies of acoustic streaming effects on microparticles/droplets in microchannel flow," Int. J. Eng. Sci. **169**, 103563 (2021).
[22]Y. Kim and C. S. Peskin, "Penalty immersed boundary method for an elastic boundary with mass," Phys. Fluids **19**, 053103 (2007).
[23]Y. Kim and C. S. Peskin, "A penalty immersed boundary method for a rigid body in fluid," Phys. Fluids **28**, 033603 (2016).
[24]T. G. Fai, B. E. Griffith, Y. Mori, and C. S. Peskin, "Immersed boundary method for variable viscosity and variable density problems using fast constant-coefficient linear solvers I: Numerical method and results," SIAM J. Sci. Comput. **35**, B1132–B1161 (2013).
[25]Y. Kim and C. S. Peskin, "Numerical study of incompressible fluid dynamics with nonuniform density by the immersed boundary method," Phys. Fluids **20**, 062101 (2008).
[26]J. Happel and H. Brenner, *Low Reynolds Number Hydrodynamics: With Special Applications to Particulate Media*, Vol. 1 (Springer Science & Business Media, 1983).
[27]M. Settnes and H. Bruus, "Forces acting on a small particle in an acoustical field in a viscous fluid," Phys. Rev. E **85**, 016327 (2012).
[28]S. Danilov and M. Mironov, "Mean force on a small sphere in a sound field in a viscous fluid," J. Acoust. Soc. Am. **107**, 143–153 (2000).
[29]P. J. Westervelt, "Acoustic radiation pressure," J. Acoust. Soc. Am. **29**, 26–29 (1957).
[30]G. T. Silva, "An expression for the radiation force exerted by an acoustic beam with arbitrary wavefront (l)," J. Acoust. Soc. Am. **130**, 3541–3544 (2011).
[31]W. L. M. Nyborg, "Acoustic streaming," in *Physical Acoustics* (Elsevier, 1965), Vol. 2, pp. 265–331.
[32]M. A. Yurkin and A. G. Hoekstra, "The discrete dipole approximation: An overview and recent developments," J. Quant. Spectrosc. Radiat. Transfer **106**, 558–589 (2007).
[33]F. G. Mitri, "Axisymmetric scattering of an acoustical Bessel beam by a rigid fixed spheroid," IEEE Trans. Ultrason, Ferroelect, Freq. Control **62**, 1809–1818 (2015).
[34]L. Wang and F.-B. Tian, "Numerical study of sound generation by three-dimensional flexible flapping wings during hovering flight," J. Fluids Struct. **99**, 103165 (2020).
[35]J. H. Seo and R. Mittal, "A high-order immersed boundary method for acoustic wave scattering and low-Mach number flow-induced sound in complex geometries," J. Comput. Phys. **230**, 1000–1019 (2011).
[36]E. H. Trinh and C.-J. Hsu, "Equilibrium shapes of acoustically levitated drops," J. Acoust. Soc. Am. **79**, 1335–1338 (1986).
[37]H. Jackson, M. Barmatz, and C. Shipley, "Equilibrium shape and location of a liquid drop acoustically positioned in a resonant rectangular chamber," J. Acoust. Soc. Am. **84**, 1845–1862 (1988).
[38]P. L. Marston, S. E. LoPorto-Arione, and G. L. Pullen, "Quadrupole projection of the radiation pressure on a compressible sphere," J. Acoust. Soc. Am. **69**, 1499–1501 (1981).
[39]J. P. Leão-Neto, J. H. Lopes, and G. T. Silva, "Acoustic radiation torque exerted on a subwavelength spheroidal particle by a traveling and standing plane wave," J. Acoust. Soc. Am. **147**, 2177–2183 (2020).
[40]J. Kim, D. Kim, and H. Choi, "An immersed-boundary finite-volume method for simulations of flow in complex geometries," J. Comput. Phys. **171**, 132–150 (2001).
[41]R. Mittal and G. Iaccarino, "Immersed boundary methods," Annu. Rev. Fluid Mech. **37**, 239–261 (2005).
[42]Y. Bao, A. Donev, B. E. Griffith, D. M. McQueen, and C. S. Peskin, "An immersed boundary method with divergence-free velocity interpolation and force spreading," J. Comput. Phys. **347**, 183–206 (2017).